Photoacoustics 46 (2025) 100776

Contents lists available at ScienceDirect

Photoacoustics

journal homepage: www.elsevier.com/locate/pacs

Radiomics-driven perfusion prediction in clinical photoacoustic foot imaging

Chuqin Huang [a], Yanda Cheng [a], Xiaoyu Zhang [b], Ye Zhan [c], Wenhan Zheng [a], Isabel Komornicki [d], Linda M. Harris [d], Wenyao Xu [b], Jun Xia [a,*]

[a] Department of Biomedical Engineering, University at Buffalo, The State University of New York, Buffalo, NY 14260, USA
[b] Department of Computer Science and Engineering, University at Buffalo, The State University of New York, Buffalo, NY 14260, USA
[c] Linde Inc., Tonawanda, NY 14150, USA
[d] Department of Surgery, University at Buffalo, The State University of New York, Buffalo, NY 14203, USA

ARTICLE INFO

Keywords:
Photoacoustic
Photoacoustic tomography
Foot imaging
Radiomics
Machine learning

ABSTRACT

Accurate assessment of tissue perfusion is essential for managing chronic foot ulcers in patients with diabetes and peripheral arterial disease. While photoacoustic (PA) imaging enables high-resolution visualization of vascular structures, current perfusion evaluation methods are limited. We propose a fully automated radiomics-based framework for predicting perfusion conditions using single-wavelength clinical PA foot imaging. Radiomics features were extracted from both raw radiofrequency (RF) signals and reconstructed maximum amplitude projection (MAP) images. After reproducibility testing and statistical filtering, features were ranked using a combined minimum redundancy maximum relevance (mRMR) and ReliefF approach. A k-nearest neighbors ensemble model trained on eight selected features achieved an area under the curve (AUC) of 0.90 (training) and 0.94 (test). The selected features corresponded with physiological indicators such as vessel density, tissue structure, and vascular discontinuity. This study demonstrates a reliable and interpretable method for perfusion assessment in PA imaging with strong clinical potential.

1. Introduction

Chronic leg wounds are a growing concern among the aging population, affecting over 6.5 million Americans and resulting in annual treatment costs of $25 billion in the United States [1–3]. These ulcers often originate from vascular diseases at both macrovascular and microvascular levels, leading to ischemia and impaired healing [4]. Revascularization surgery is an effective intervention that restores arterial blood flow to ulcers [5]. However, in patients with diabetes or peripheral arterial disease, perfusion may be adequate in one vessel but insufficient in areas of tissue loss [5,6], highlighting the need for accurate perfusion assessment to optimize patient care.

Current clinical tests for assessing blood perfusion remain inadequate [2]. Generalized approaches such as the ankle–brachial index (ABI) and toe–brachial index (TBI) cannot resolve perfusion within specific tissue regions and are limited by vessel calcification, loss of digits, and operator variability [7]. Photoplethysmography (PPG) is affected by skin conditions [8], and transcutaneous oxygen pressure (TcPO2) requires prolonged acquisition times and is influenced by edema or cellulitis [9]. Doppler ultrasound primarily evaluates proximal vessels, with low sensitivity to microvasculature [7]. X-ray computed tomography (CT) angiography has ionizing radiation and contrast agent injection. Magnetic resonance angiography (MRA) offers high-resolution vascular imaging but is limited by long scan times, high cost, and often the need for gadolinium-based contrast [2]. Near-infrared fluorescence angiography with indocyanine green (ICG) can visualize tissue perfusion, but clinical use is constrained by the need for contrast injection [9].

Photoacoustic (PA) tomography (PAT) is an emerging modality based on photoacoustic effect, which enables mapping of the optical absorption through acoustic detection [10–13]. By overcoming the diffusion limit inherent in traditional optical imaging, PAT can generate high-resolution images in deep tissues, as acoustic waves experience significantly less attenuation than light. Leveraging these advancements, PAT shows great potential for both preclinical research and clinical practice across diverse fields [14], including but not limited to breast cancer diagnosis [15–17], palm biometric extraction [18], thyroid cancer detection [19], lymphatic disease monitoring [20], and

* Corresponding author.
E-mail address: junxia@buffalo.edu (J. Xia).

https://doi.org/10.1016/j.pacs.2025.100776
Received 18 August 2025; Received in revised form 8 October 2025; Accepted 21 October 2025
Available online 24 October 2025

melanoma diagnosis [21].

Recent studies have demonstrated the potential of PAT systems to predict perfusion conditions using PAT images. Choi et al. reported that total hemoglobin concentration, hemoglobin oxygen saturation, and vessel density could accurately describe the microvascular change due to venous occlusion [22], but these findings were based on healthy volunteers experiments only. Yang et al. evaluated vascular function through post-occlusive reactive hyperemia [23], but the occlusion process could be painful and potentially harmful for patients with peripheral artery disease. Wang et al. used the vessel-to-background ratio as an indicator of perfusion [24], while Huang et al. proposed an integrated index combining vessel density, occupancy, and sharpness for perfusion estimation [25]. Huynh et al. found vessel tortuosity to be strongly associated with peripheral vessel disease [26]. However, the accuracy of these evaluation metrics often depends on reliable vessel segmentation. In addition, further validation might be necessary due to the limited sample sizes in these studies. Mantri et al. proposed that the rate of PA intensity change could indicate the angiogenesis rate [27]. However, the intensity-only analysis is subject to laser-dependent fluctuations and excitation light conditions.

Radiomics is a rapidly evolving field in medical imaging, leveraging data-characterization algorithms to extract a wide range of quantitative features, which are often beyond human visual detection [28]. It has been increasingly applied to medical imaging modalities such as magnetic resonance imaging, ultrasound, and computed tomography, uncovering critical insights for disease classification and prognosis [28, 29]. Recently, radiomics has also been adapted for both in-vivo and ex-vivo photoacoustic imaging, highlighting its potential to enhance diagnostic capabilities [30–33]. This approach offers a transformative opportunity to predict perfusion conditions more effectively by providing a detailed and comprehensive analysis of PA imaging data.

In this study, we present a fully automated radiomics-based approach for predicting perfusion conditions using single-wavelength clinical PA foot imaging. The method involves extracting a comprehensive set of radiomics features from both raw radiofrequency (RF) signals and reconstructed maximum amplitude projection (MAP) images acquired by a portable single-wavelength PA system. Key features are identified through a systematic selection process that includes reproducibility testing, statistical filtering, and feature ranking. These selected features are then used to train machine learning models for classifying perfusion status. Notably, the extracted features are interpretable and exhibit clear associations with physiological indicators of perfusion, such as vessel density, tissue architecture, and vascular discontinuity. This approach not only improves prediction accuracy but also deepens the understanding of the relationship between PA signals and perfusion conditions, providing valuable insights to support clinical decision-making.

2. Methods

2.1. Workflow

The proposed workflow consists of four main stages: preprocessing, feature extraction, feature selection, and model evaluation, as shown in Fig. 1. During preprocessing, regions of interest (ROIs) are automatically generated from both the PA RF data and the reconstructed MAP images using a customized automatic segmentation algorithm. In the feature extraction stage, first-order statistical and texture features are computed from both data types using the PyRadiomics library [34], with various image filters applied to enhance feature diversity and representation. Feature selection is carried out through a series of steps, including a reproducibility test, the Mann–Whitney *U* test with Bonferroni correction, correlation analysis, and feature importance ranking. Subsequently, machine learning models including k-nearest neighbors (KNN) ensemble, support vector machine (SVM), and random forest are trained using the selected features. Model performance is evaluated using the area under the curve (AUC) metric to identify the optimized model. In addition, we examine the physiological relevance of selected features to understand their associations with perfusion-related characteristics.

2.2. Data acquisition

The PAT images in this study were acquired through a portable imaging system proposed in [25]. The experimental setup of the imaging system was presented in Fig. 2. As demonstrated in Fig. 2(a), the scanning head of the system consists of a customized linear-array transducer (Imasonics SAS, France) with 128 elements and 2.25 MHz central frequency, a fiber bundle, a high-performance cold mirror (Edmund Optics Inc), and a 3D-printed base. The transducer has an 86-mm total length to cover the foot. The transducer and fiber bundle head are placed vertically to each other, with the cold mirror attached at a 45-degree to fiber bundle. This design achieves co-planar light illumination and acoustic detection, optimizing the imaging depth of the system. To ensure that the scanner head aligns with the surface of the foot dorsum, we used a manual rotation stage mounted at the top of the scanning head. The stage helped to reduce variation in the lateral distances to foot surface. An adjustable footrest plate is fixed under the water tank to provide proper support for the subject's foot to improve the imaging stability. A

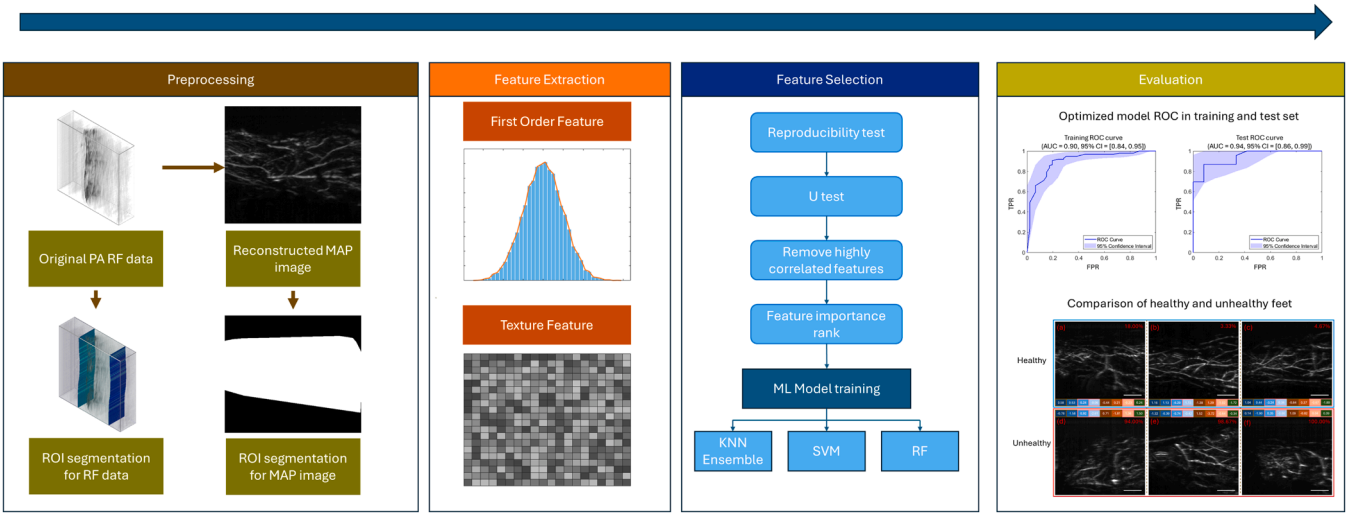

Fig. 1. Workflow of the study.

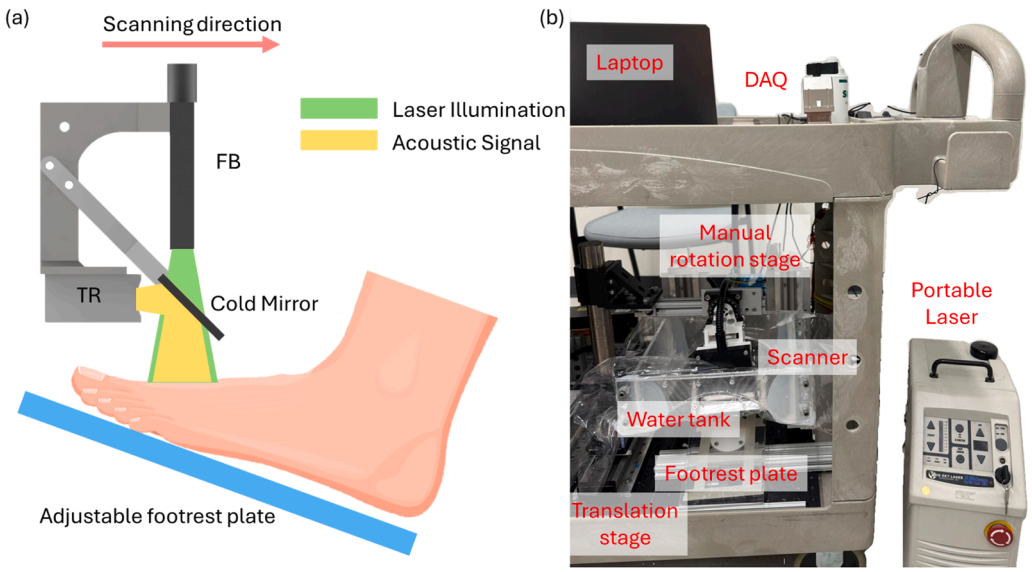

Fig. 2. Experimental setup of the clinical photoacoustic imaging system. (a). A schematic drawing of the imaging system. The light illumination is marked in green, while the acoustic propagation is labeled in yellow. (b) A photograph of the imaging system. Most equipment of the system is installed on a cart, except for the portable laser.

10 Hz portable laser (Big Sky Laser) is employed to provide photoacoustic excitation, and a portable data acquisition (DAQ) unit (Photosound Technologies Inc.) is used to digitize PA signals with a 40 MHz sampling rate. A photo of the imaging system is shown in Fig. 2(b). Most equipment of the system is installed in a cart, except for the portable laser. Exemplary PA vascular images of feet can be found in

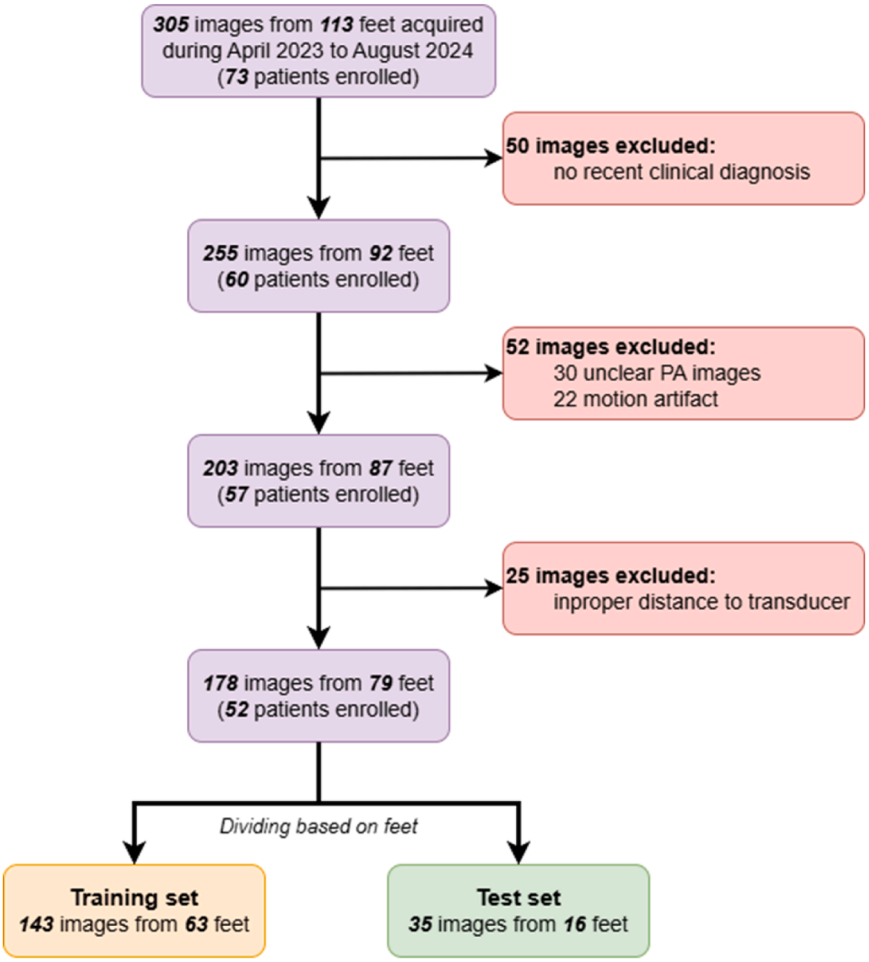

Fig. 3. A flowchart illustrating the process of images selection.

Supplementary Material Fig. S1.

Approval of all ethical and experimental procedures and protocols was granted by the Institutional Review Boards of the University at Buffalo under Protocol No. STUDY00001165 in Oct 2017. All human subjects provided informed consent after fully understanding the implications of their participation.

From April 2023 to August 2024, a total of 305 PA images were acquired from 113 feet of 73 patients recruited by clinical collaborators. As illustrated in Fig. 3, inclusion and exclusion criteria were systematically applied to ensure reliable data quality. First, 50 images were excluded because the corresponding patients did not have recent clinical diagnostic records. During clinical data collection, a small number of acquisitions resulted in invalid or unusable PA images due to challenging patient conditions or environmental factors. For instance, some samples showed extremely weak or absent PA signals or lacked visible vascular structures within the imaging region. We have used the quality score in Supplementary material Fig. S2 to identify these unclear PA images. Together with 22 images affected by motion artifacts, a total of 52 images were excluded at this stage. Subsequently, 25 additional images were removed due to an improper distance between the foot surface and the transducer, which can distort signal accuracy. After confirming the clinical report and image data quality, 178 images from 79 feet (52 patients) were included for feature extraction and analysis. The final dataset was divided based on feet into a training set (143 images from 63 feet) and a test set (35 images from 16 feet).

We reviewed medical records and physician notes, considered diagnostic results including Ankle-Brachial Index (ABI) and Toe-Brachial Index (TBI), and visually inspected the foot for the presence of wounds or ulcers. A foot was labeled as unhealthy if clinical diagnosis or vascular tests indicated evidence of ongoing peripheral arterial disease or if visible wounds were present. Conversely, a subject was labeled as healthy if the clinical evaluation, ABI/TBI results, and visual inspection showed no signs of disease or foot wounds.

The clinical characteristics of enrolled patients were presented in Table 1. Among 79 enrolled feet from 52 patients, 25 feet were classified as healthy and 54 feet as unhealthy. The median age across all feet was 65 years (interquartile range [58, 72.25]), with no significant difference between healthy and unhealthy groups ($p = 0.2492$). Laterality was balanced, with 38 (48 %) left feet and 41 (52 %) right feet ($p = 0.6370$). The gender distribution was 36 male (46 %) and 42 female (54 %) and likewise showed no significant group difference ($p = 0.4349$). In terms of race, 66 feet (84 %) were White, 12 (15 %) African American, and 1 (1 %) other; again, no difference between groups ($p = 0.2269$). Ulcer presence was seen in 22 feet (28 %) and was significantly more common in the unhealthy group (41 % vs. 0 %, $p = 0.0002$). P-value in Table 1 is calculated by *U* test for continuous variables and Chi-Squared test for categorical variables.

Table 1
Clinical characteristics of the recruited patients.

Variable	Total (n = 79 feet)	Healthy feet (n = 25)	Poor perfusion feet (n = 54)	P-value
Age (years), median [Q1, Q3]	65 [58, 72.25]	69.5 [58, 80.5]	65 [57.75, 72]	0.2492
Laterality, n (%)				0.6370
Left foot	38 (48 %)	13 (52 %)	25 (46 %)	
Right foot	41 (52 %)	12 (48 %)	29 (54 %)	
Gender, n (%)				0.4349
Male	36 (46 %)	13 (52 %)	23 (43 %)	
Female	42 (54 %)	12 (48 %)	31 (57 %)	
Race, n (%)				0.2269
White	66 (84 %)	19 (76 %)	47 (87 %)	
African American	12 (15 %)	5 (20 %)	7 (13 %)	
Other	1 (1 %)	1 (4 %)	0 (0 %)	
Ulcer Present, n (%)	22 (28 %)	0 (0 %)	22 (41 %)	0.0002

2.3. Data preprocessing

2.3.1. ROI segmentation for RF data

To enhance the reproducibility and repeatability of the study, we developed an automatic algorithm to label the ROIs in RF data. Considering the existence of the electromagnetic inference (EMI) noise, the wavelet filter was first applied to the RF data to improve the contrast. We then utilized the Hilbert transformation to compute the envelope of the bipolar-shaped RF signals. To simplify the analysis, each frame was compressed into a 1D array by summing the RF data along the lateral direction, followed by smoothing using a moving mean filter along axial direction to reduce noise.

Given that foot tissue exhibits significantly stronger PA responses than water, potential peaks were identified in the 1D array based on a minimum prominence of 25 % of the maximum value. To ensure consistency, peaks were refined by considering their locations across adjacent frames. The starting point of the ROI was defined as the first point exceeding 20 % of the peak height on the peak's rising edge. The axial depth of the ROI was fixed at 1000 pixels (approximately 38.5 mm) to preserve maximum information.

In this study, the raw RF data were laterally summed into a one-dimensional axial profile to enable efficient and robust detection of tissue boundaries. This approach focuses on the axial signal distribution, while lateral variation was minimized by aligning the scanning head with the foot dorsum using a rotation stage.

Notably, while extensive processing was conducted to extract ROIs, the raw bipolar RF data was saved for feature extraction to maintain data integrity.

2.3.2. MAP image reconstruction and ROI segmentation

The acquired RF signals were initially filtered by a 2–5 MHz bandpass filter and then reconstructed with the delay-and-sum method [35]. In our current workflow, the reconstruction process already utilizes information from the ROIs identified in the RF data. Specifically, the axial start point for reconstruction is set at the upper boundary of the ROIs identified in the RF data and the end point was calculated automatically based on the end depth and view angle. This process enables automatic and consistent reconstruction without manual intervention, thereby improving the reproducibility and repeatability of the study. To minimize variations caused by differing skin tones and the presence of hair, the reconstructed images underwent skin layer removal using SL-Net [36]. The investigation on the performance of skin removal procedure was presented in Supplementary material (Fig. S3). The reconstructed data was then normalized by scaling the intensity values to a range between 0 and 1, compensating for the optical attenuation caused by skin layers with different skin tones.

Given the system's large scanning window (86 mm laterally and 100 mm in the elevational direction), the foot occupies only a portion of the image in most cases. To focus solely on the features of foot tissues, we developed an automated method to extract the ROI of the foot for further processing. The skin-removed reconstructed image was fed into a 3D FD-UNet to suppress noise and enhance vasculature [37]. Following enhancement, vessels in the MAP image were segmented by applying a threshold set to the 95th percentile of the image's histogram. Although this high threshold excluded some smaller vessels, the primary vasculature was reserved. A convex hull was subsequently generated from the binarized vessels to define the ROI for the MAP image. A more detailed workflow of ROI selection was presented in the Workflow for ROIs Selection and Fig. S4 in the Supplementary Material.

2.4. Radiomic feature extraction

To extract radiomic features, we utilized the Pyradiomics library, an open-source and widely adopted platform that provides standardized tools for reproducible feature extraction. Prior to the feature extraction, several image filters were applied to ensure a comprehensive analysis of

both RF data and reconstructed MAP images. The application of a diverse range of filters enriched the variety of extracted features by highlighting distinct image properties such as intensity, texture, edges, and multiscale patterns. This approach enhanced the sensitivity and robustness of radiomics analysis, enabling improved characterization of complex image data while reducing biases associated with raw intensity values.

To discretize gray levels in the RF data and MAP images, we set a bin width of 25 for MAP images and 1000 for RF data. Additionally, to optimize computational efficiency, the RF data was down sampled by a factor of four, reducing the sampling frequency from 40 MHz to 10 MHz. According to the Nyquist-Shannon sampling theorem, a 10 MHz sampling frequency is sufficient to retain meaningful information for a transducer with a central frequency of 2.25 MHz.

For both original and filtered images, features from various feature classes were extracted for each image type. Specifically, 18 first-order features (histogram statistics) were computed to describe the intensity distribution of voxels within the ROI [38,39]. Furthermore, 73 texture features from calculated from several matrices, including 22 features from Gray-level Cooccurrence Matrix (GLCM) [40], 16 features Gray-level Run-length Matrix (GLRLM) [41], 16 features from Gray-level Size Zone Matrix (GLSZM) [42], 5 features from Neighboring Gray Tone Difference Matrix (NGTDM) [43] and 14 features from Gray-level Dependence Matrix (GLDM) [44]. It is notable that features extracted from MAP images and raw RF data are different. Specifically, MAP images were treated as 2D data while RF data were treated as 3D volumes, and distinct image filters were applied during preprocessing to enhance feature diversity in each domain. These features provide a comprehensive representation of intensity and texture patterns within the data. The image filters used in this study are summarized in Supplementary Material Table S1.

2.5. Dataset splitting

The dataset was divided into training and test sets using a stratified sampling approach to preserve the proportion of healthy and unhealthy cases in both subsets. To avoid data leakage, the split was performed based on individual feet, ensuring that samples originating from the same foot were assigned exclusively to either the training set or the test set. The division followed an 80:20 ratio, with 80 % of the data allocated to the training set and the remaining 20 % to the test set. The samples in the test sets were used for model evaluation only and were not involved in feature selection or machine learning model training.

2.6. Feature selection

2.6.1. Reproducibility examination

Considering that some radiomics features are sensitive to image acquisition and processing settings [45], we examined features extracted from different samples but acquired from the same foot on the same date to verify the reproducibility. The coefficient of variation (CV) was applied to estimate the variance between features from samples obtained from the same foot on the same date. The calculated CV was averaged among subjects, and the final threshold for the average CV was set as 0.1. Features with CV larger than this value were considered as poor reproducible and were not enrolled in the following analysis. This procedure aims to eliminate features sensitive to small variations.

2.6.2. Initial feature filtering with U test

After removing poorly reproducible features, we would like to discover features which contain important information about blood perfusion. Therefore, we implemented the Mann-Whitney-Wilcoxon test (*U* test) to identify the potential features related to the perfusion condition [46]. Since there were a large number of features involved in the *U* test, Bonferroni correction was adopted in this study to adjust p-values to account for multiple comparisons and control the risk of false positives [47]. The significance level was set at 0.05, features with adjusted p-values lower than the threshold were considered as significantly related to the perfusion condition and initially selected for further processing.

2.6.3. Correlation analysis

Considering the large number of extracted features, there is a high possibility that some features correlate with each other. The presence of highly correlated features can lead to redundancy and multicollinearity, especially for studies with a relatively small dataset. We conducted a correlation analysis for features selected by the *U* test by computing the pair-wise Pearson's correlation coefficient (PCC) [48]. In this study, we set the correlation coefficient threshold at 0.8 to consider the feature pairs highly related. For these highly related feature pairs, we selected the most important feature determined by their p-value. Removing these correlated features contributes to improved model stability, interpretability and performance.

2.6.4. Feature ranking

To identify the most relevant features for tissue perfusion, we employed a comprehensive feature selection process combining minimum Redundancy Maximum Relevance (mRMR) [49], and ReliefF algorithms [50]. These two methods assess feature importance from relevance with minimal redundancy and neighborhood-based relevance, respectively. The feature importance was evaluated by these two methods independently. An integrated ranking was then computed for each feature by summing its ranks estimated by the two methods. Features were subsequently ordered by their integrated scores with lower scores indicating higher overall importance.

A backward search was initialized to identify the optimized combinations of features for perfusion prediction. Starting from the set containing all features involved, each searching step will remove the least important feature based on their ranking, until only the most significant feature is used for building the machine learning model. This method evaluated features in multiple aspects, making the feature ranking robust and computationally efficiency for this task.

2.6.5. Machine learning model construction

Based on filtered features, we implemented three machine learning models: k-nearest neighbors (KNN) ensemble [51], support vector machine (SVM) [52], and random forest [53]. Model training was conducted using a five-fold cross-validation strategy to prevent overfitting.

The primary metric used for model evaluation was the area under the receiver operating characteristic curve. AUC was selected for its ability to assess the model's discriminatory power across all classification thresholds, providing a comprehensive measure of performance. The comparative analysis of the AUC values obtained from the KNN ensemble, SVM, and random forest models enabled the identification of the most effective approach for radiomics analysis.

In the aforementioned workflow, the skin removal (SL-Net), vessel enhancement (3D FDUNet), and radiomics feature extraction were conducted in Python (Python Software Foundation) with version 3.8.19. Other processing and analysis were implemented in MATLAB R2022b (MathWorks Inc.). Details of the hyperparameters can be found in the Supplementary Materials section.

3. Results

3.1. ROIs segmentation for both MAP images and RF data

We applied the automatic segmentation algorithm to all samples in the dataset to define the ROIs. ROI selection is a critical step in radiomics analysis because accurate segmentation ensures that the extracted features are truly representative of the target tissue, allowing for more precise characterization and prediction of disease conditions. To evaluate the performance of the segmentation algorithm, we randomly

selected several samples for visual inspection, as shown in Fig. 4.

The top row of Fig. 4 presents representative MAP images with red contours indicating the segmented ROIs generated by our proposed method. The results show that the ROIs closely follow the anatomical structures of the foot while successfully excluding irrelevant background areas, demonstrating high segmentation accuracy. The bottom row of Fig. 4 displays 3D renderings of the raw RF data. We adjusted the alpha map parameters to display low-amplitude signals and applied generic depth weighting to compensate for optical and acoustic attenuation in deeper tissue regions. These adjustments were used only for rendering and did not affect the data used for feature extraction or analysis. In these renderings, the blue stripe-like regions represent the automatically identified top and bottom boundaries of the segmented ROIs. These boundaries effectively restrict the ROI to the regions containing tissue PA signals.

The consistent segmentation performance observed across different samples in both MAP images and RF data underscores the robustness and reliability of the proposed algorithm. This ensures that only the relevant foot tissue regions are retained for the subsequent radiomics feature extraction process.

3.2. Feature extraction

We performed feature extraction on both the MAP images and RF data using the generated ROI masks, ensuring that all first-order statistical features and texture features were derived from the imaged tissue regions. In total, 1023 features were extracted from the MAP images, and 1092 features were extracted from the RF data for each sample. The difference in the number of features is due to the application of different image filters and the dimensionality of the data: the RF data were treated as 3D volumes, whereas the MAP images were processed as 2D pixel-based images.

3.3. Reproducibility test result

To eliminate radiomic features that are sensitive to minor variations, we assessed feature stability using the average CV. The quantified CV values of the extracted features are shown in Fig. 5(a), while the distribution of CV values is illustrated in the histogram in Fig. 5(b). A black dashed line in the figure indicates the CV threshold (0.1) used to identify poorly reproducible features. Based on this criterion, we identified and excluded 653 features with low reproducibility. The remaining 1462 features were retained for further analysis.

The main causes affecting the reproducibility of these 653 features are background, noise, and small variations in the scanning region. The applied Pyradiomics library extracts a comprehensive radiomic feature set from MAP image and RF data. However, some of the features focus on the image background and noise, which vary in every experiment. Also, some features are sensitive to small variations in scanning regions. Therefore, these features present poor performance in reproducibility tests.

3.4. P-value filtering by U test

We applied the Mann–Whitney *U* test with Bonferroni correction to identify features that showed statistical significance in predicting perfusion conditions. The adjusted p-values of the features are shown in Fig. 6(a), where the threshold for statistical significance is indicated by a black dashed line. In Fig. 6(a), background colors represent the types of image filters applied, and different marker shapes indicate feature classes. Additionally, features extracted from RF data and MAP images are distinguished by a top banner. To enhance visualization, the y-axis of Fig. 6(a) represents the negative logarithm of the adjusted p-values, and therefore higher y-axis values correspond to greater statistical significance. Based on this analysis, 20 features were identified as statistically significant for perfusion prediction and were selected for further evaluation.

3.5. Removal of highly correlated features

We examined the correlation among the significant features identified through the *U* test to detect highly related feature pairs. The heatmap of the Pearson's correlation coefficients is shown in Fig. 6(b), where feature pairs with strong correlations are highlighted by black rectangles. Based on this analysis, 6 highly correlated features were removed to reduce redundancy, and the remaining 14 features were retained for constructing the prediction models.

3.6. Integrated feature ranking and model performance analysis

Feature importance was evaluated using an integrated score derived from the mRMR method and the ReliefF algorithm. A backward search strategy was then applied to determine the optimal subset of features. The AUC values obtained from several machine learning models trained with different numbers of features are shown in Fig. 7(a1). In general, model performance improved as more features were included, with the KNN ensemble consistently outperforming SVM and random forest models in most cases.

Based on the highest AUC achieved on the training set, the KNN ensemble model using the 8 most significant features was selected as the

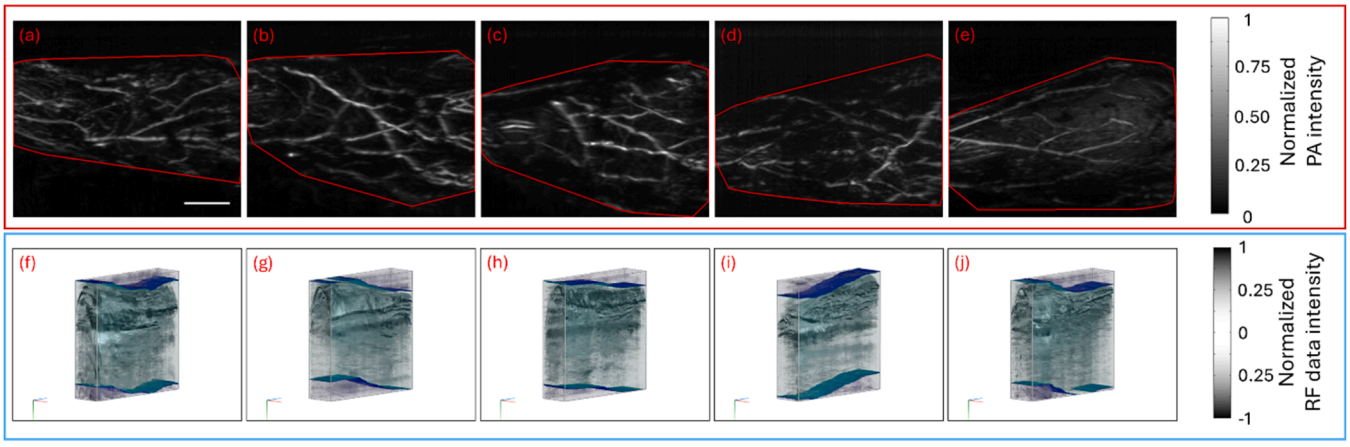

Fig. 4. ROI segmentation demonstration of multiple samples. Top row (a to e) presents MAP images, and red contours indicate the segmented ROI by the proposed method. Bottom row (f to j) displays 3D raw RF data renderings, and blue stripe-like regions label the automatically identified top and bottom boundaries of the segmented ROIs. Scale bar: 20 mm.

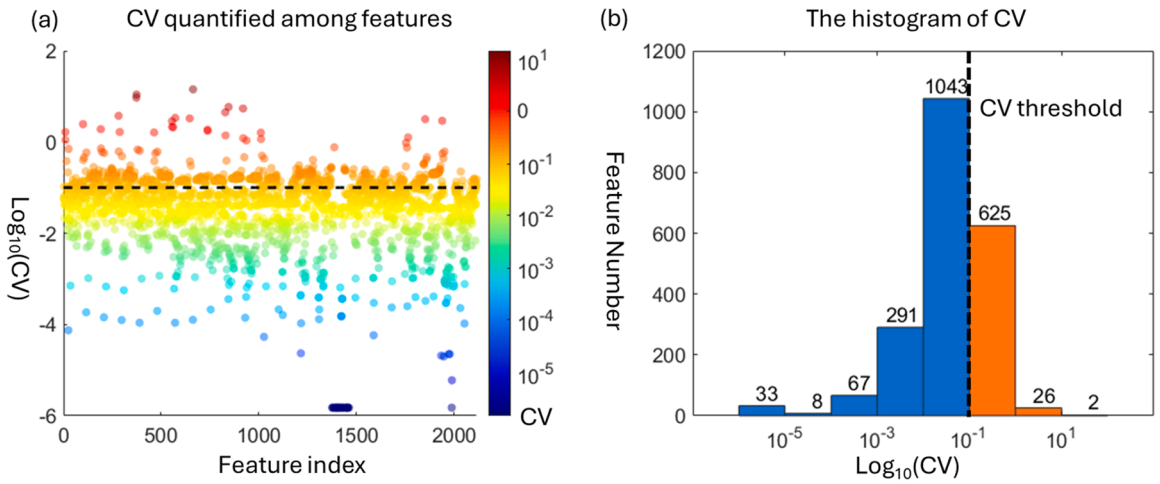

Fig. 5. Quantified coefficient of variation (CV) analysis of the features. (a) A scatter plot demonstrating the quantified CV among features. (b) The histogram of calculated CV. We applied logarithm transformation to CV in (b) for a better illustration. The threshold for considering the feature as poor-reproducible was set at 10^{-1} and was labeled by the black dashed line.

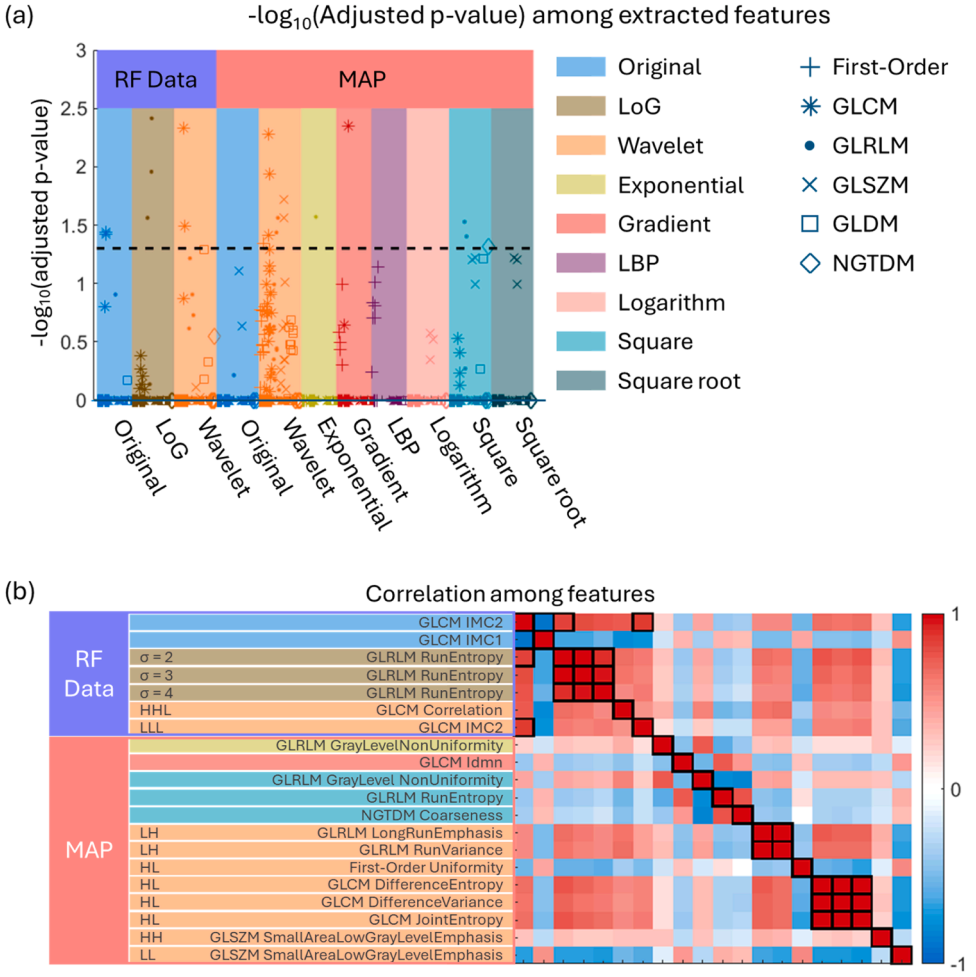

Fig. 6. Statistical significance and correlation analysis of extracted radiomic features from RF data and MAP images. (a) Quantified p-value of features by *U* test. Notably, the y-axis was set as -$\log_{10}$(p-value) for a better illustration. The p-value threshold of significance was set at 0.05 and was marked by black dashed line. (b) The Pearson's correlation heatmap of significant features. Higher related feature pairs were marked by a black rectangle, and feature names were labeled at the left side of the figure. The same legend was used for image filters in (a) and (b).

optimized model. This selection is indicated by a black arrow in Fig. 7 (a1). To further evaluate its performance, we plotted the receiver operating characteristic (ROC) curves for the training and test sets in Fig. 7(a2) and Fig. 7(a3), respectively. The optimized model achieved an AUC of 0.90 (95 % confidence interval: 0.84–0.95) on the training set and an AUC of 0.94 (95 % confidence interval: 0.86–0.99) on the test set.

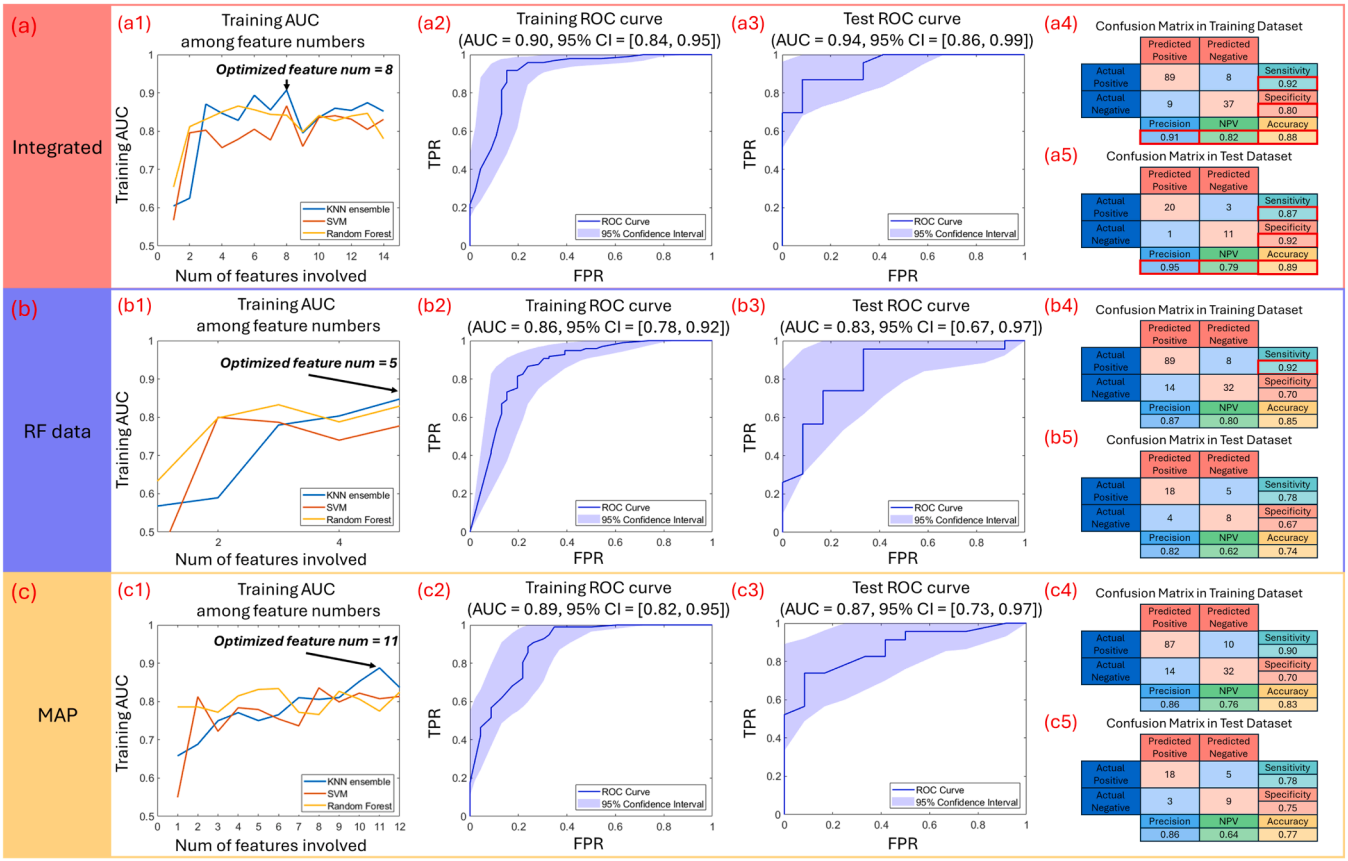

Fig. 7. Performance comparison of machine learning models trained on different feature sets. (a) Integrated features from both RF data and MAP images. (b) Features from RF data only. (c) Features from MAP images only. For each model, the first column ((a1) – (c1)) shows training AUC among the number of features involved, with the optimized feature number indicated by a black arrow. The second ((a2) – (c2)) and third columns ((a3) – (c3)) show ROC curves for training and test set, with corresponding AUC values and 95 % confidence intervals. The fourth column ((a4) – (c4) and (a5) – (c5)) presents confusion matrices summarizing classification performance on training and test sets. CI: Confidence interval; FPR: False positive rate; TPR: True positive rate; NPV: Negative predictive value.

These results demonstrate the model's strong ability to distinguish poor perfusion conditions from healthy foot tissue.

The confusion matrices of the optimized model for the training and test sets are shown in Fig. 7(a4) and (a5), respectively. The model demonstrated strong classification ability, with high sensitivity and specificity, indicating effective identification of both poor and good perfusion conditions. Precision was consistently high, reflecting a low false positive rate. The model also maintained stable accuracy across datasets and provided reliable negative predictive values. These results confirm that the proposed model achieves robust and generalizable performance, supporting its potential utility in clinical applications for perfusion condition prediction.

To evaluate the benefit of combining features from both RF data and MAP images, we repeated the same workflow using features from each data source independently. Results are shown in Fig. 7(b1–b5) for RF data and Fig. 7(c1–c5) for MAP images. The RF-based model selected five features and achieved AUCs of 0.86 (training) and 0.83 (test), as shown in Fig. 7(b2) and 7(b3). The MAP-based model, optimized with eleven features, reached AUCs of 0.89 (training) and 0.87 (test), shown in Fig. 7(c2) and 7(c3). Confusion matrices in Fig. 7(b4–b5) and Fig. 7 (c4–c5) indicate lower accuracy and predictive values compared to the integrated model, although sensitivity and specificity remained acceptable. These results suggest that combining RF and MAP features captures complementary information and leads to improved classification performance and model generalizability.

3.7. Comparison with other methods

To further validate the performance of the proposed method, we conducted a comprehensive comparison using evaluation metrics from various models. The top row of Fig. 8(a)–(d) displays the ROC curves for different models under various conditions to assess diagnostic accuracy. The bottom row, Fig. 8(e)–(h), shows the corresponding decision curve analysis (DCA) results, which evaluate clinical utility and net benefit. In all subfigures, the red bold curve represents the optimized model selected in this study.

The first column of Fig. 8 presents a direct comparison between the optimized model and SVM and random forest models trained on the same feature subset. The optimized model outperformed both SVM and random forest in terms of AUC and net benefit, consistent with previous findings.

For a more comprehensive comparison, we applied the Least Absolute Shrinkage and Selection Operator (LASSO) with five-fold cross-validation to identify significant features. LASSO is a widely used regularization technique that performs both variable selection and regularization, helping to reduce overfitting by applying an L1 penalty. In this analysis, two feature subsets were generated based on the LASSO minimum mean squared error (minMSE) point and the one standard error (1SE) point. Multiple models including the original LASSO model, KNN ensemble, SVM, and random forest were constructed using each LASSO-derived feature set. Their performance, shown in the second and third columns of Fig. 8, demonstrates that the optimized model proposed in this study achieved better performance compared to all LASSO-based models.

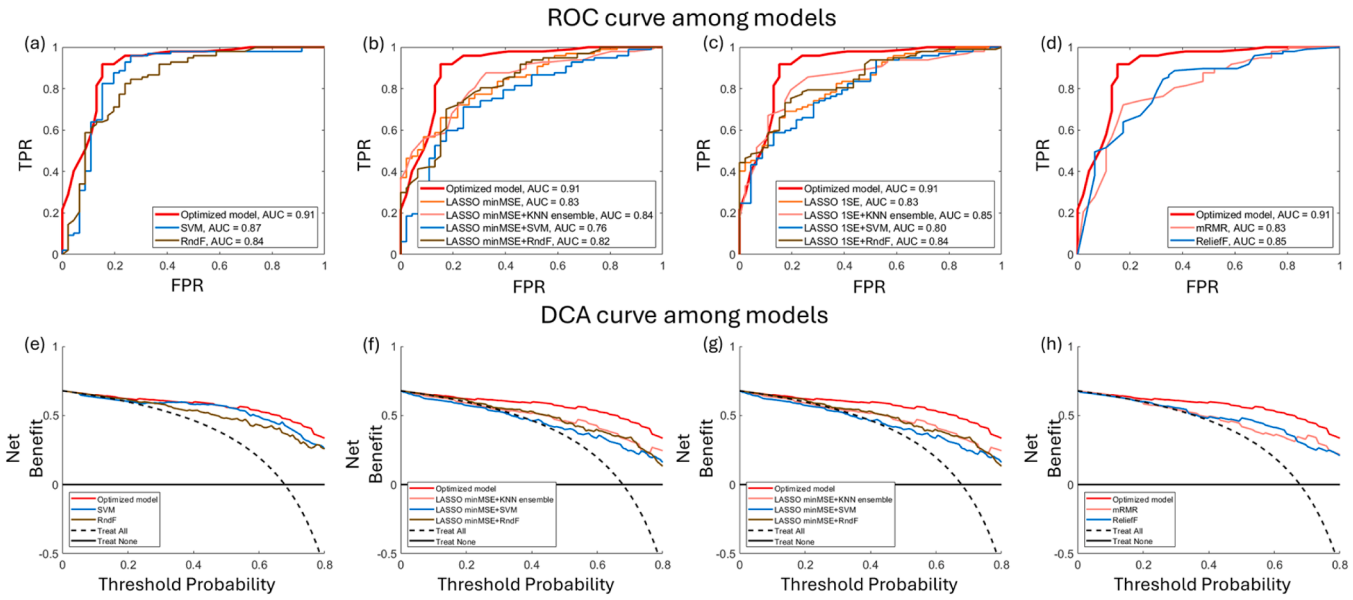

Fig. 8. ROC and DCA from models built under various conditions. The top row of the figure presents the ROC curve and the bottom row displays DCA. The red curve represents the optimized model in all subfigures. RndF: random forest.

We also evaluated the effectiveness of the proposed integrated scoring approach. The fourth column of Fig. 8 compares the performance of KNN ensemble models built on features selected using the integrated scoring method, mRMR alone, and ReliefF alone. The results indicate that the integrated scoring method leads to superior performance compared to either individual method.

3.8. *Physiological representation of selected features*

The optimized model achieved the best performance compared to other models, showing great potential to be deployed for clinical decision making. To investigate the physiological representations of selected features, three pairs of samples comparing healthy and unhealthy feet were demonstrated in Fig. 9. For each column of the figure, samples were collected from the same subject on the same date. The MAP images of healthy feet were presented in the top row in the blue box while images from unhealthy feet were shown in the bottom row in the red box. The predicted probability of unhealthy from the optimized model was marked in the top right corner. Meanwhile, we listed z-score normalized feature values for each image. Feature values were listed in tables following the order: GLCM Informational Measure of Correlation (IMC) 1 in RF data, Laplacian of Gaussian (LoG) (sigma=4.0 mm) 3D GLRLM Run Entropy in RF data, gradient GLCM Inverse Difference Moment Normalized (IDMN) in MAP image, wavelet HL GLCM Joint Entropy in MAP image, wavelet HHL GLCM Correlation in RF data, wavelet LLL GLCM IMC2 in RF data, wavelet LL GLSZM Small Area Low Gray Level Emphasis in MAP image, and square GLRLM Run Entropy in MAP image. These features were labeled as F1 to F8 for better discussion.

We categorized these features into three groups based on our observations and comparison of PA images and quantified feature values from healthy and unhealthy feet. Feature values in each group were filled with blue, brown, and green, respectively.

Firstly, we observed that healthy feet usually have greater vessel

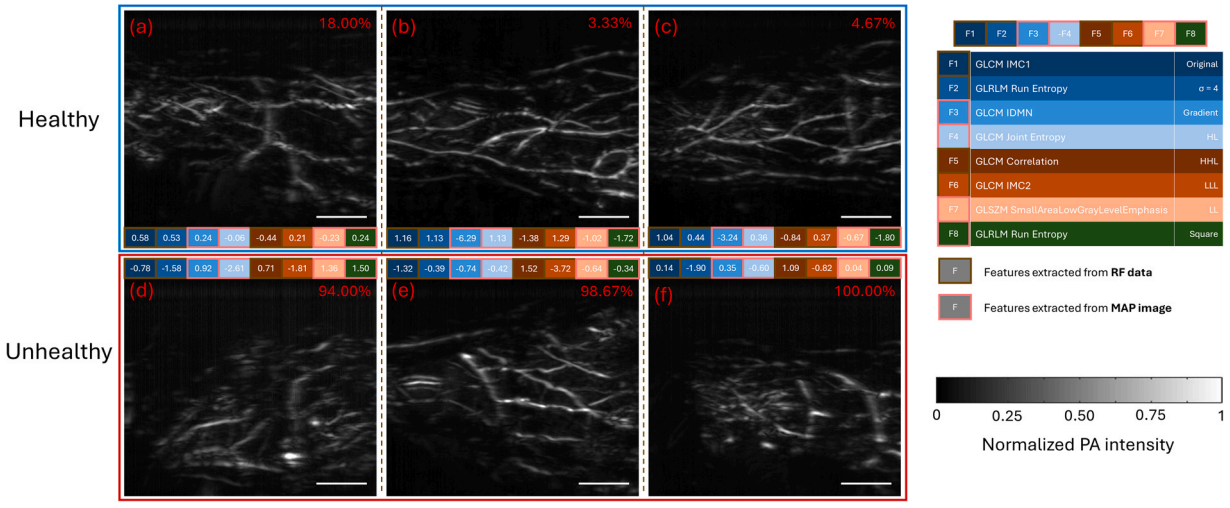

Fig. 9. Representative MAP images and feature distributions from healthy and unhealthy feet. Images of healthy feet were presented in the top row (blue box) while images from unhealthy feet were shown in the bottom row (red box). The predicted probability of unhealthy was marked in the top right corner in red for each case. The table adjacent to MAP images lists z-score normalized feature values. The annotations of each value are presented on the right side of the figure. Scale bar: 20 mm.

density, which can be validated by four extracted features (features in blue cells). Feature GLCM IMC1 in RF data (F1) reflects correlation and dependency in texture patterns, and we observed F1 has a higher value in healthy feet, indicating greater global structural complexity which can be caused by more vessels. Feature LoG (sigma = 4.0 mm) 3D GLRLM Run Entropy in RF data (F2) quantifies randomness of runs in edge-enhanced RF data, and it also has higher value in healthy feet, demonstrating that healthy foot exhibits more complex edge information, indicative of more vessels and sharper structures compared to unhealthy feet. Feature gradient GLCM IDMN in MAP image (F3) has a higher value in unhealthy feet, suggesting that unhealthy feet exhibit more homogeneous local gradients and reduced rapid changes due to fewer vessels. Feature HL GLCM Joint Entropy in MAP image (F4) has a higher value in healthy feet. Elevated joint entropy indicates that more vessels in healthy feet contribute to texture complexity.

Secondly, we can also observe abnormal or ischemia tissue conditions in unhealthy feet according to feature analysis (features in brown boxes). Feature HHL GLCM Correlation in RF data (F5) measures linear dependency between pixel intensities in the HHL wavelet band. We found higher correlation values in unhealthy feet, suggesting a more rapid change in high-frequency RF data from unhealthy feet, which indicates disrupted or irregular textures. Meanwhile, Feature LLL GLCM IMC2 (F6) quantifies uniformity or predictability in texture patterns at a coarse scale. The analysis demonstrates that it has a greater value in healthy feet, which shows healthy feet have more intact and organized tissue structures. Feature LL GLSZM Small Area Low Gray Level Emphasis (F7) estimated small zones with low gray level intensities in smoothed MAP images, and results pointed out that unhealthy feet have higher feature value compared to healthy feet. It indicates a greater number of small zones with low intensity in unhealthy foot tissue regions, which might be due to ischemia tissue.

Besides, we also noticed there are more discontinued vessels in unhealthy feet. It can be proved by feature square GLRLM Run Entropy in MAP (F8, in green cell) which measures diversity in run lengths and gray level combinations in intensity-enhanced images. Unhealthy feet have greater feature value, demonstrating that vessel structures in unhealthy feet are more heterogeneous and less continuous, which aligns with reports of interrupted or disrupted vessels in feet with poor perfusion [26]. A summary of the physiological representation of features can be found in the supplementary material Tables S2 and S3.

In Fig. 9, feature analysis reveals consistent patterns between the extracted feature values and visual observations from the images. In MAP images of healthy feet (Fig. 9(a) to (c)), dense and continuous vascular networks are clearly visible. For example, in Fig. 9(b), features F1 and F2 reach their maximum values, while F3 reaches its minimum, indicating a complex vascular structure with well-defined edges and strong local gradients resulting from the rich vasculature. In contrast, MAP images of unhealthy feet exhibit distinct alterations. In Fig. 9(d), the vessel network appears sparse, consistent with low F1 and F2 values. At the same time, high F7 and F8 values correspond to blurred vessel boundaries and discontinuous structures, suggesting impaired vessel integrity and the presence of small ischemic tissue regions. In Fig. 9(e), although a relatively dense and sharp vascular network is present, the vessels appear tortuous and exhibit variable brightness along their paths (with bright spots on the vessels). This visual pattern aligns with the highest F5 and lowest F6 values, which are indicative of irregular texture patterns. Such tortuous vessel morphology may reflect the development of collateral (bypass) micro vessels in response to major vessel occlusion, a compensatory mechanism previously reported in ischemic tissues [54]. Finally, Fig. 9(f) shows poorly defined vessels, consistent with the lowest F2 and elevated F5 values, reflecting a loss of edge information and signs of tissue disruption. Overall, these findings demonstrate that the extracted radiomics features effectively capture physiological alterations associated with perfusion status in clinical PA foot imaging.

4. Discussion

In this study, we propose a radiomics-based method to predict the perfusion condition of foot ulcer patients using clinically acquired PA images. The automated workflow begins with the preprocessing of the acquired data, followed by the extraction of radiomics features from both the raw RF data and the reconstructed MAP images. These features are subsequently refined through a reproducibility test, the *U* test, and correlation analysis. We then ranked the importance of features using a proposed integrated score that combines the mRMR method and the ReliefF algorithm. A prediction model was built based on eight selected features. The optimized model achieved an AUC of 0.90 on the training set and 0.94 on the test set, demonstrating its effectiveness in accurately predicting perfusion conditions from PA images. Additionally, we compared the optimized model with alternative models developed using different feature selection strategies by evaluating both AUC and DCA. The results indicate that the optimized model outperformed the others in classification performance and provided the highest clinical utility.

Since there is no widely accepted and publicly available clinical PA foot imaging dataset, we constructed a dataset consisting of over 300 clinical samples from more than 100 unique feet. Compared to previous studies that were limited by small sample sizes or conducted only on healthy volunteers, our dataset offers significant advantages for developing machine learning models. These advantages include improved model accuracy, reduced overfitting, and enhanced generalization.

We extracted over 2000 radiomics features from both 3D RF data and 2D reconstructed MAP images, providing a comprehensive and diverse feature set. Unlike traditional metrics such as vessel density or vessel occupancy, radiomics features can capture subtle image characteristics that are not easily detected by the human eye. These hidden features, often associated with tissue heterogeneity and underlying biological changes, can offer valuable insights into disease processes. Furthermore, features extracted directly from RF data may contain more informative content, as reconstruction algorithms can potentially discard important details.

The entire workflow, including preprocessing, feature extraction and selection, and model building, is fully automatic. This removes human involvement and greatly improves the method's consistency and reliability. Notably, the optimized model achieved high AUC and great clinical net benefit, indicating strong predictive performance for assessing perfusion conditions and highlighting its potential for clinical application. Additionally, we analyzed the physiological representations of the selected features and found that the optimized model primarily focused on vessel density, abnormal tissue structures, and disrupted vessels to make predictions.

Despite the encouraging results, there are still several limitations that can be addressed in future work. Firstly, the dataset used in this study, while being the largest in photoacoustic-based foot imaging, is still much smaller than radiomic studies in other medical imaging modalities [52]. The limited data size may affect the generalizability of the findings. This limitation can be mitigated by continuing clinical data collection to expand the dataset. Secondly, the current model is restricted to binary classification due to the absence of detailed clinical scoring as ground truth. This issue could be addressed by incorporating transcutaneous oxygen pressure ($TcPO_2$) measurements, which would provide quantitative reference values for perfusion assessment and enable more nuanced classification. Finally, the lack of longitudinal study design prevents the evaluation of perfusion changes over time. Future studies incorporating longitudinal data would be valuable for tracking disease progression and assessing the temporal dynamics of perfusion status.

5. Conclusion

In summary, this study presents a radiomics-based framework for predicting perfusion conditions in foot tissues using PA imaging. By

extracting over 2000 quantitative features from both raw RF data and reconstructed MAP images acquired with a single-wavelength portable PA system, our method captures complex image patterns that are difficult to detect visually. A fully automated workflow was implemented, encompassing data preprocessing, reproducibility testing, statistical filtering, and feature selection using an integrated scoring method. The optimized KNN ensemble model, trained on 8 selected features, achieved an AUC of 0.90 on the training set and 0.94 on the test set. The selected features revealed meaningful associations with perfusion-related physiological changes, such as vessel density, tissue irregularity, and vascular discontinuity. The proposed approach demonstrates strong predictive performance and clinical relevance, offering a robust and interpretable solution for perfusion assessment in photoacoustic foot imaging.

CRediT authorship contribution statement

Chuqin Huang: Writing – original draft, Methodology, Investigation, Data curation, Conceptualization. **Yanda Cheng:** Investigation, Data curation. **Linda M. Harris:** Resources. **Wenyao Xu:** Supervision, Resources, Funding acquisition. **Jun Xia:** Writing – review & editing, Supervision, Project administration, Funding acquisition, Conceptualization. **Xiaoyu Zhang:** Software, Resources. **Ye Zhan:** Writing – review & editing. **Wenhan Zheng:** Methodology. **Isabel Komornicki:** Resources.

Declaration of Competing Interest

The authors declare the following financial interests/personal relationships which may be considered as potential competing interests: Jun Xia reports financial support was provided by National Institutes of Health. If there are other authors, they declare that they have no known competing financial interests or personal relationships that could have appeared to influence the work reported in this paper.

Acknowledgment

This work was supported by the National Institute of Health [Grants R01EB029596, R01EB028978, and R01EB035188].

Appendix A. Supporting information

Supplementary data associated with this article can be found in the online version at doi:10.1016/j.pacs.2025.100776.

Data Availability

Data will be made available on request.

References

[1] C.K. Sen, G.M. Gordillo, S. Roy, R. Kirsner, L. Lambert, T.K. Hunt, F. Gottrup, G. C. Gurtner, M.T. Longaker, Human skin wounds: a major and snowballing threat to public health and the economy, Wound Repair Regen. 17 (6) (2009) 763–771.
[2] K.F. Ma, S.F. Kleiss, R.C. Schuurmann, R.P. Bokkers, Ç. Ünlü, J.-P.P. De Vries, A systematic review of diagnostic techniques to determine tissue perfusion in patients with peripheral arterial disease, Expert Rev. Med. Devices 16 (8) (2019) 697–710.
[3] G. FrykbergRobert, Challenges in the treatment of chronic wounds, Adv. Wound Care (2015).
[4] O.A. Mennes, J.J. van Netten, R.H. Slart, W. Steenbergen, Novel optical techniques for imaging microcirculation in the diabetic foot, Curr. Pharm. Des. 24 (12) (2018) 1304–1316.
[5] C.E. Attinger, K.K. Evans, E. Bulan, P. Blume, P. Cooper, Angiosomes of the foot and ankle and clinical implications for limb salvage: reconstruction, incisions, and revascularization, Plast. Reconstr. Surg. 117 (7S) (2006) 261S–293S.
[6] B.E. Sumpio, R.O. Forsythe, K.R. Ziegler, J.G. van Baal, M.J. Lepantalo, R. J. Hinchliffe, Clinical implications of the angiosome model in peripheral vascular disease, J. Vasc. Surg. 58 (3) (2013) 814–826.
[7] R.G. Frykberg, J. Banks, Challenges in the treatment of chronic wounds, Adv. Wound Care 4 (9) (2015) 560–582.
[8] J. Allen, Photoplethysmography and its application in clinical physiological measurement, Physiol. Meas. 28 (3) (2007) R1.
[9] M. Venermo, N. Settembre, A. Albäck, P. Vikatmaa, P.-S. Aho, M. Lepäntalo, Y. Inoue, H. Terasaki, Pilot assessment of the repeatability of indocyanine Green fluorescence imaging and correlation with traditional foot perfusion assessments, Eur. J. Vasc. Endovasc. Surg. 52 (4) (2016) 527–533.
[10] L.V. Wang, S. Hu, Photoacoustic tomography: in vivo imaging from organelles to organs, Science 335 (6075) (2012) 1458–1462.
[11] J. Xia, J. Yao, L.V. Wang, Photoacoustic tomography, Princ. Adv. Electro Waves 147 (2014) 1–22.
[12] L.V. Wang, H.-i Wu, Biomedical Optics: Principles and Imaging, John Wiley & Sons, 2012.
[13] M. Xu, L.V. Wang, Photoacoustic imaging in biomedicine, Rev. Sci. Instrum. 77 (4) (2006).
[14] L. Lin, L.V. Wang, The emerging role of photoacoustic imaging in clinical oncology, Nat. Rev. Clin. Oncol. 19 (6) (2022) 365–384.
[15] L. Lin, P. Hu, J. Shi, C.M. Appleton, K. Maslov, L. Li, R. Zhang, L.V. Wang, Single-breath-hold photoacoustic computed tomography of the breast, Nat. Commun. 9 (1) (2018) 2352.
[16] N. Nyayapathi, R. Lim, H. Zhang, W. Zheng, Y. Wang, M. Tiao, K.W. Oh, X.C. Fan, E. Bonaccio, K. Takabe, Dual scan mammoscope (DSM)—a new portable photoacoustic breast imaging system with scanning in craniocaudal plane, IEEE Trans. Biomed. Eng. 67 (5) (2019) 1321–1327.
[17] H. Zhang, E. Zheng, W. Zheng, C. Huang, Y. Xi, Y. Cheng, S. Yu, S. Chakraborty, E. Bonaccio, K. Takabe, OneTouch automated photoacoustic and ultrasound imaging of breast in standing pose, IEEE Trans. Med. Imaging (2025).
[18] W. Zheng, D. Lee, J. Xia, Photoacoustic tomography of fingerprint and underlying vasculature for improved biometric identification, Sci. Rep. 11 (1) (2021) 17536.
[19] B. Park, C. Kim, J. Kim, Recent advances in ultrasound and photoacoustic analysis for thyroid cancer diagnosis, Adv. Phys. Res. 2 (4) (2023) 2200070.
[20] S. Van Heumen, J.J. Riksen, M.K.A. Singh, G. Van Soest, D. Vasilic, LED-based photoacoustic imaging for preoperative visualization of lymphatic vessels in patients with secondary limb lymphedema, Photoacoustics 29 (2023) 100446.
[21] J.W. Fakhoury, J.B. Lara, R. Manwar, M. Zafar, Q. Xu, R. Engel, M.M. Tsoukas, S. Daveluy, D. Mehregan, K. Avanaki, Photoacoustic imaging for cutaneous melanoma assessment: a comprehensive review, J. Biomed. Opt. 29 (S1) (2024). S11518-S11518.
[22] W. Choi, E.-Y. Park, S. Jeon, Y. Yang, B. Park, J. Ahn, S. Cho, C. Lee, D.-K. Seo, J.-H. Cho, Three-dimensional multistructural quantitative photoacoustic and US imaging of human feet in vivo, Radiology 303 (2) (2022) 467–473.
[23] J. Yang, G. Zhang, Q. Shang, M. Wu, L. Huang, H. Jiang, Detecting hemodynamic changes in the foot vessels of diabetic patients by photoacoustic tomography, J. Biophoton. 13 (8) (2020) e202000011.
[24] Y. Wang, Y. Zhan, L.M. Harris, S. Khan, J. Xia, A portable three-dimensional photoacoustic tomography system for imaging of chronic foot ulcers, Quant. Imaging Med. Surg. 9 (5) (2019) 799.
[25] C. Huang, Y. Cheng, W. Zheng, R.W. Bing, H. Zhang, I. Komornicki, L.M. Harris, P. R. Arany, S. Chakraborty, Q. Zhou, Dual-scan photoacoustic tomography for the imaging of vascular structure on foot, IEEE Trans. Ultrason. Ferroelectr. Freq. Control (2023).
[26] N. Huynh, E. Zhang, O. Francies, F. Kuklis, T. Allen, J. Zhu, O. Abeyakoon, F. Lucka, M. Betcke, J. Jaros, A fast all-optical 3D photoacoustic scanner for clinical vascular imaging, Nat. Biomed. Eng. (2024) 1–18.
[27] Y. Mantri, J. Tsujimoto, B. Donovan, C.C. Fernandes, P.S. Garimella, W.F. Penny, C. A. Anderson, J.V. Jokerst, Photoacoustic monitoring of angiogenesis predicts response to therapy in healing wounds, Wound Repair Regen. 30 (2) (2022) 258–267.
[28] R.J. Gillies, P.E. Kinahan, H. Hricak, Radiomics: images are more than pictures, they are data, Radiology 278 (2) (2016) 563–577.
[29] H.J. Aerts, E.R. Velazquez, R.T. Leijenaar, C. Parmar, P. Grossmann, S. Carvalho, J. Bussink, R. Monshouwer, B. Haibe-Kains, D. Rietveld, Decoding tumour phenotype by noninvasive imaging using a quantitative radiomics approach, Nat. Commun. 5 (1) (2014) 4006.
[30] B.L. Bungart, L. Lan, P. Wang, R. Li, M.O. Koch, L. Cheng, T.A. Masterson, M. Dundar, J.-X. Cheng, Photoacoustic tomography of intact human prostates and vascular texture analysis identify prostate cancer biopsy targets, Photoacoustics 11 (2018) 46–55.
[31] J. Kang, W.Y. Chung, S.-W. Kang, H.J. Kwon, J. Yoo, E.-K. Kim, J.H. Chang, T.-k Song, S. Lee, J.Y. Kwak, Ex vivo estimation of photoacoustic imaging for detecting thyroid microcalcifications, PLoS One 9 (11) (2014) e113358.
[32] L. Escudero Sanchez, E. Brown, L. Rundo, S. Ursprung, E. Sala, S.E. Bohndiek, I. X. Partarrieu, Feasibility and sensitivity study of radiomic features in photoacoustic imaging of patient-derived xenografts, Sci. Rep. 12 (1) (2022) 15142.
[33] G. Li, Z. Huang, H. Luo, H. Tian, Z. Ding, Y. Deng, J. Xu, H. Wu, F. Dong, Photoacoustic imaging radiomics to identify breast cancer in BI-RADS 4 or 5 lesions, Clin. Breast Cancer (2024).
[34] J.J. Van Griethuysen, A. Fedorov, C. Parmar, A. Hosny, N. Aucoin, V. Narayan, R. G. Beets-Tan, J.-C. Fillion-Robin, S. Pieper, H.J. Aerts, Computational radiomics system to decode the radiographic phenotype, Cancer Res. 77 (21) (2017) e104–e107.
[35] C. Hoelen, F. De Mul, R. Pongers, A. Dekker, Three-dimensional photoacoustic imaging of blood vessels in tissue, Opt. Lett. 23 (8) (1998) 648–650.
[36] C. Huang, E. Zheng, W. Zheng, H. Zhang, Y. Cheng, X. Zhang, V. Shijo, R.W. Bing, I. Komornicki, L.M. Harris, Enhanced clinical photoacoustic vascular imaging

through a skin localization network and adaptive weighting, Photoacoustics (2025) 100690.
[37] W. Zheng, H. Zhang, C. Huang, V. Shijo, C. Xu, W. Xu, J. Xia, Deep learning enhanced volumetric photoacoustic imaging of vasculature in human, Adv. Sci. (2023) 2301277.
[38] A. Zwanenburg, S. Leger, M. Vallières, S. Löck, Image biomarker standardisation initiative, arXiv preprint arXiv:1612.07003, 2016.
[39] H. Benoit-Cattin, Texture analysis for magnetic resonance imaging, Texture Anal. Magn. Reson. (2006).
[40] R.M. Haralick, K. Shanmugam, I.H. Dinstein, Textural features for image classification, IEEE Trans. Syst. Man Cybern. (6) (1973) 610–621.
[41] M. Galloway, Texture classification using gray level run length, Comput. Graph. Image Process 4 (2) (1975) 172–179.
[42] G. Thibault, J. Angulo, F. Meyer, Advanced statistical matrices for texture characterization: application to cell classification, IEEE Trans. Biomed. Eng. 61 (3) (2013) 630–637.
[43] M. Amadasun, R. King, Textural features corresponding to textural properties, IEEE Trans. Syst. Man Cybern. 19 (5) (1989) 1264–1274.
[44] C. Sun, W.G. Wee, Neighboring gray level dependence matrix for texture classification, Comput. Vis. Graph. Image Process. 23 (3) (1983) 341–352.
[45] A. Zwanenburg, Radiomics in nuclear Medicine: robustness, reproducibility, standardization, and how to avoid data analysis traps and replication crisis, Eur. J. Nucl. Med. Mol. Imaging 46 (13) (2019) 2638–2655.
[46] J.D. Gibbons, S. Chakraborti, Nonparametric Statistical Inference: Revised and Expanded, CRC press, 2014.
[47] E.W. Weisstein, Bonferroni correction, https://mathworld. wolfram. com/, 2004.
[48] F. Galton, Typical Laws of Heredity, William Clowes and Sons, 1877.
[49] C. Ding, H. Peng, Minimum redundancy feature selection from microarray gene expression data, J. Bioinforma. Comput. Biol. 3 (02) (2005) 185–205.
[50] M. Robnik-Šikonja, I. Kononenko, Theoretical and empirical analysis of ReliefF and RReliefF, Mach. Learn. 53 (2003) 23–69.
[51] T.K. Ho, The random subspace method for constructing decision forests, IEEE Trans. Pattern Anal. Mach. Intell. 20 (8) (1998) 832–844.
[52] N. Cristianini, An Introduction to Support Vector Machines and Other Kernel-based Learning Methods, Cambridge University Press, 2000.
[53] L. Breiman, Random forests, Mach. Learn. 45 (2001) 5–32.
[54] A.N. Keeling, T.J. Carroll, M.M. McDermott, K. Liu, Y. Liao, C.T. Farrelly, W. H. Pearce, J. Carr, Clinical correlates of size and number of collateral vessels in peripheral artery disease, Vasc. Med. 17 (4) (2012) 223–230.

Chuqin Huang Department of Biomedical Engineering, University at Buffalo, Buffalo, New York, USA Chuqin Huang is a Ph.D. student in the biomedical Engineering department at University at Buffalo, the State University of New York. He received the B.E. degree in Mechanical Engineering from Huazhong University of Science and Technology in 2018, and the M.S. degree in Mechanical Engineering from University at Washington in 2020. His research includes photoacoustic tomography and its application on foot imaging.

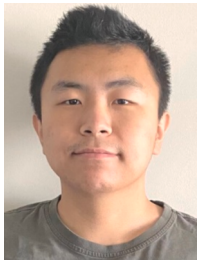

Yanda Cheng Department of Biomedical Engineering, University at Buffalo, Buffalo, New York, USA Yanda Cheng is a Ph. D. student in the Biomedical Engineering Department at the University at Buffalo, the State University of New York. He received his Bachelor of Science degree in Electrical Engineering from the University of Kentucky in 2020 and received his Master of Science degree in Biomedical Engineering from Cornell University in 2021. Yanda's research focuses on photoacoustic imaging, deep learning, machine learning, and image processing.

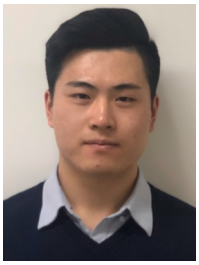

Xiaoyu Zhang Department of Computer Science and Engineering, University at Buffalo, Buffalo, New York, USA Xiaoyu Zhang received the engineering degree from Hefei University of Technology, China, in 2017, the Master degree in engineering from the University of Science and Technology of China, China, in 2020, and now he is pursuing the Ph.D. degree in computer science from the State University of New York at Buffalo, United States. His current research interests include Wireless Sensing, Internet of Things (IoT) and Smart Health.

Ye Zhan Linde Inc., Tonawanda, New York, USA Holding a PhD in biomedical engineering and with over five years of industrial experience, Ye specializes in developing optical and ultrasound-based biosensing and biometric technologies, with over 20 publications, and award-winning health tech innovations.

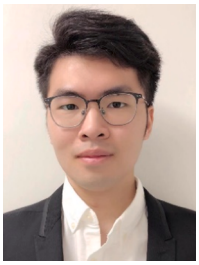

Wenhan Zheng Department of Biomedical Engineering, University at Buffalo, Buffalo, New York, USA Dr. Wenhan Zheng received his doctorate in the Biomedical Engineering Department at the University at Buffalo, the State University of New York. Dr. Zheng has over ten publications in peer-reviewed journals, specifically focusing on the field of photoacoustics. Furthermore, he has acquired substantial industry experience by working with leading global companies in his field.

Isabel Komornicki Department of Surgery, University at Buffalo, Buffalo, New York, USA Isabel Komornicki, MSN, NP, Nurse Practitioner with the University at Buffalo Surgeons for the past 16 years in the department of surgery, vascular department. She received her Bachelors and Masters of science in Nursing at SUNY at Buffalo. She is primarily active in the outpatient clinical settings; treating vascular patients in all phases of disease. She has also participated in numerous research projects throughout her career, involving medical devices, pharmaceuticals and novel immunotherapies related vascular and connective tissue disorders. Currently, she is a research coordinator with the SUNY at Buffalo Research Foundation, in addition to clinical practice.

Linda M. Harris Department of Surgery, University at Buffalo, Buffalo, New York, USA Dr. Linda M Harris is a tenured Professor of Surgery in the Department of Surgery, Division of Vascular Surgery at the Jacobs School of Medicine and Biomedical Sciences, University at Buffalo. She is previous Chief of the Division of Vascular Surgery, and is currently the program director for the vascular training programs. She has been practicing in Buffalo for over 25 years since completing her general surgery and vascular surgery training at the University of Buffalo. Dr Harris has coedited 2 books, written over 20 book chapters, and published well over 100 peer reviewed publications on a wide variety of vascular diseases. She has served as President of the Eastern Vascular Society and the Association of Program Directors in Vascular Surgery. Her research interests include Peripheral arterial disease, including diagnostic assessment.

Wenyao Xu Department of Computer Science, University at Buffalo, Buffalo, New York, USA Wenyao Xu (M'13-SM'18) received a Ph.D. degree from the University of California, Los Angeles, CA, USA, in 2013. He received both an M.S. degree in 2008 and a B.S. degree in 2006 from Zhejiang University, China (both with honors). Currently, Dr. Xu is a Professor at the Computer Science and Engineering Department, the State University of New York (SUNY) at Buffalo, New York, NY, USA. He published over 230 technical papers, co-authored 2 books, and is named inventor on nine International and U.S. patents. His recent research foci include the Internet of Things, Smart Health, and Cyber-Security, and his work has received 11 Best Paper Awards in related research fields. Dr. Xu has served on the technical program committee of numerous conferences in the field of Smart Health, Mobile Computing and the Internet of Things, and has been a TPC co-chair of IEEE BSN 2018/2023 and IEEE/ACM CHASE 2022.

Jun Xia Department of Biomedical Engineering, University at Buffalo, Buffalo, New York, USA Dr. Jun Xia, Ph.D., is a Professor in the Biomedical Engineering Department at University at Buffalo, the State University of New York. He received his doctorate in Mechanical Engineering from the University of Toronto and postdoctoral training in Biomedical Engineering at Washington University in St. Louis. Dr. Xia has published three book chapters and more than seventy papers in peer-reviewed journals on photoacoustic research.